Influence of thermal gradient and vapor content of landfill gas on water storage in the loess-gravel cover

Guangyao Li, Liangtong Zhan & Wenjie Xu
MOE Key Laboratory of Soft soils and Geoenvironmental Engineering, Zhejiang University, Hangzhou, China

ABSTRACT: Temperature and relative humidity of the landfill gas (LFG) at the bottom and surface of a loess-gravel cover were measured, and vapor content of the LFG was obtained based on the measured data. Numerical simulations were conducted to investigate the influence of thermal gradient and vapor content of the LFG on the moisture movement and water storage in the cover. Results indicated that thermal gradient caused moisture movement from the higher-temperature zone to the lower-temperature zone by means of vaporization and condensation. The thermally induced increase of water storage in the upper part of the cover can accelerate the evaporation at the cover surface, leading to decreasing the water storage in the whole cover. The maximum decrease of the available water storage caused by thermal gradient for a whole year was 16 mm, and the maximum increase of the available water storage caused by vapor content of the LFG for a whole year was 30 mm.

1 INTRODUCTION

The soil covers at landfills are usually unsaturated under natural climate conditions. Water could be further stored in and landfill gas (LFG) could migrate through the voids of the unsaturated soil (Mbonimpa et al. 2003; Spokas et al. 2011). Therefore, the water storage in the soil cover has a significant influence on its performance at limiting percolation and LFG emission.

The bottom of the cover contacts directly with the underlying high temperature waste. Previous results indicated that the maximum waste temperatures of 60 to 70 °C were measured in anaerobic zone (Dach and Jager 1995). That indicates that thermal gradient would be formed between the upper and lower boundary of the cover. Thermal gradient may lead to the moisture movement in the soil cover, which can subsequently affect the water distribution and storage in the soil cover. In the past decades, engineering experiences have indicated that thermally induced moisture movement had a significant influence on the facilities, even can result in a structural failure. Li et al (2014) investigated the thermally induced moisture movement in the subsurface soil, which may lead to severe nonuniform settlement and frost heave of the road. Brachman et al (2014) investigated the downslope bentonite erosion from a geosynthetic clay liner (GCL) caused by the diurnal temperature cycles. However, currently there is a lack of researches focusing on the moisture movement in the soil covers due to thermal gradient at landfills. On the other hand, the vapor content of the LFG generated from the underlying waste is quite high because of the high temperature and water content of the waste. This quantity of the vapor also has a potential to condense in the cover subjected to thermal gradient, leading to increase the water storage in the cover. However, the effect of the vapor of LFG has never been considered in previous studies. These limitations impede a better understanding and evaluation of the performance of the soil cover.

At Jiangcungou landfill in Xi'an city of China, the temperature and relative humidity of the LFG at the bottom and surface of the loess-gravel cover were measured, and then the vapor contents of the LFG were calculated based on the measured data. Numerical simulations were performed to investigate the properties of moisture movement subjected to different thermal gradients and vapor contents of the LFG. Results can provide beneficial guidance to evaluate the performance of the loess-gravel cover.

2 FIELD MEASUREMENTS OF THE VAPOR CONTENT OF THE LFG

The field measurements were conducted on Jiangcungou landfill at Xi'an city, China, and the loess-gravel cover was adopted for the landfill. The thickness of the loess and gravel layer were 0.9-3.0 m and 0.3 m, respectively, as shown in Fig. 1. Perforated pipes were installed inside the gravel layer to collect and transport the generated LFG. The collected LFG could be released to the atmosphere through the vertically placed imperforated pipes, as shown in Fig 1a, which will be called the LFG escape-pipes in this paper. Figure. 1b shows the cross section of the loess-gravel cover as well as the testing points for a pair of test. Each pair of test consisted of two testing points, including the surface and bottom testing point. Bottom testing points were located at the bottom of the LFG escape-pipes and surface testing points were located at the surface of the cover around the LFG escape-pipes. There were totally 17 pairs of test, including 34 testing points.

Figure 1. Information about the test site: (a) LFG escape-pipe; (b) Cross section of the loess-gravel cover and testing points

A digital hygrothermograph (SSN-22E) was utilized to measure the temperature and relative humidity of the LFG at the testing points. The hygrothermograph consisted of a recorder and an external probe, and a 5 m long data cable was connected between the recorder and the probe as shown in Fig. 2. The test range of temperature was from -40 to 100 ℃ with an error of ± 0.3 ℃. The test range of relative humidity was from 0 to 100 % with an error of ± 3 %.

Figure 2. Digital hygrothermograph (SSN-22E)

The vapor content of the LFG (unit: g/kg) is defined as the quantity of the vapor (unit: g) coexisting with 1 kg dry LFG. The vapor content of the LFG can be calculated based on the temperature and relative humidity.

$$d = 1000\frac{m_{H_2O}}{m_{LFG} - m_{H_2O}} = 1000\frac{P_{H_2O}}{P_{LFG} - P_{H_2O}} \cdot \frac{M_{H_2O}}{M_{LFG-H_2O}} \quad (1)$$

Where P_{H_2O} is the pressure of the vapor, $P_{H_2O}=RH\times P_{H_2O,\max}$, RH is the relative humidity of the wet LFG, $P_{H_2O,\max}$ is the saturated vapor pressure, which is a temperature dependent parameter; P_{LFG} is the pressure of the wet LFG, which was taken as 1atm in this study; M_{H_2O} and M_{LFG-H_2O} are the molar mass of the vapor and dry LFG, respectively. M_{H_2O} =18g/mol; M_{LFG-H_2O} could be roughly calculated as 16×0.6+44×0.4=27.2 g/mol by assuming that the dry LFG was composed of only CH_4 and CO_2 with a ratio of 6:4.

The calculated vapor content of the LFG using Eq. (1) is presented in Fig. 3, in which the theoretical maximum vapor content was obtained by assuming the relative humidity of the LFG equaled 100%. It can be found that the vapor content of the LFG at bottom of the cover was close to the theoretical maximum vapor content, which was attributed to the high relative humidity of the bottom LFG. The vapor content of the LFG at bottom of the cover increased significantly with the increase of the temperature. While, for the LFG at surface of the cover, the vapor content remained relatively stable with the variation of the temperature. The vapor content of the LFG at bottom of the cover was much higher than that of the surface for a given temperature. This demonstrated that the vapor gradually transformed into liquid water (i.e., condensation) when the LFG migrated through the cover under thermal gradient.

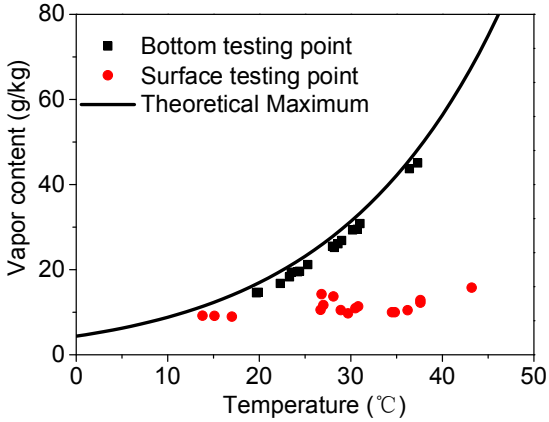

Figure 3. Calculated vapor contents of the LFG

3 NUMERICAL SIMULATIONS

3.1 *Governing equations*

In this study, an OpenGeoSys model involving the heat transport and multi-phase flow processes was established. Heat transfer through conduction and convection was well considered in the model. The water phase was assumed to be incompressible and its phase change (evaporation and condensation) was considered. The gas phase was assumed to be compressible and obeyed the ideal gas law. In particular, the gas phase was modelled as an ideal gas composed of dry air and water vapor. The water and gas flow was described using Darcy's law. The diffusion of vapor was involved in this model and described by Fick's law. The mass conservation equation for water and vapor is expressed as follows (Sanavia et al. 2005):

$$\begin{aligned} & n\left[\rho^{\mathrm{w}}-\rho^{\mathrm{gw}}\right]\left[\frac{\partial S_{\mathrm{w}}}{\partial p^{\mathrm{c}}}\frac{\partial p^{\mathrm{c}}}{\partial t}\right]+\left[1-S_{\mathrm{w}}\right]n\left[\frac{\partial \rho^{\mathrm{gw}}}{\partial p^{\mathrm{c}}}\frac{\partial p^{\mathrm{c}}}{\partial t}\right] \\ & -\mathrm{div}\left(\rho^{\mathrm{g}}\frac{M_{\mathrm{a}}M_{\mathrm{w}}}{M_{\mathrm{g}}^{2}}\boldsymbol{D}\mathrm{grad}\left(\frac{p^{\mathrm{gw}}}{p^{\mathrm{c}}}\right)\right) \\ & +\mathrm{div}\left(\rho^{\mathrm{w}}\frac{\boldsymbol{k}k^{\mathrm{rw}}}{\mu^{\mathrm{w}}}\left[-\mathrm{grad}(p^{\mathrm{g}})+\mathrm{grad}(p^{\mathrm{c}})+\rho^{\mathrm{w}}\boldsymbol{g}\right]\right) \\ & +\mathrm{div}\left(\rho^{\mathrm{gw}}\frac{\boldsymbol{k}k^{\mathrm{rg}}}{\mu^{\mathrm{g}}}\left[-\mathrm{grad}(p^{\mathrm{g}})+\rho^{\mathrm{g}}\boldsymbol{g}\right]\right)=0 \end{aligned} \quad (2)$$

where n is porosity; S_w is saturation of water; $\boldsymbol{k}$ is intrinsic permeability tensor, and k^{rw} and k^{rg} are relative permeability of the water phase and gas phase. μ^w is viscosity of water phase; M_a, M_w, and M_g are molar mass of the dry air phase, water phase, and gas phase, respectively; p^{gw} is partial pressure of water vapor; $\boldsymbol{g}$ is the gravity acceleration. ρ^w, ρ^{gw} *and* ρ^g are the density of the water, vapor, and gas phase, respectively.

The mass conservation equation for the dry air is written as:

$$\begin{aligned}
&-n\rho^{\mathrm{ga}}\left[\frac{\partial S_{\mathrm{w}}}{\partial T}\frac{\partial T}{\partial t}+\frac{\partial S_{\mathrm{w}}}{\partial p^{\mathrm{c}}}\frac{\partial p^{\mathrm{c}}}{\partial t}\right]\\
&+[1-S_{\mathrm{w}}]n\left[\frac{\partial \rho^{\mathrm{ga}}}{\partial T}\frac{\partial T}{\partial t}+\frac{\partial \rho^{\mathrm{ga}}}{\partial p^{\mathrm{c}}}\frac{\partial p^{\mathrm{c}}}{\partial t}+\frac{\partial \rho^{\mathrm{ga}}}{\partial p^{\mathrm{g}}}\frac{\partial p^{\mathrm{g}}}{\partial t}\right]\\
&-\mathrm{div}\left(\rho^{\mathrm{g}}\frac{M_{\mathrm{a}}M_{\mathrm{w}}}{M_{\mathrm{g}}^2}\boldsymbol{D}\mathrm{grad}\left(\frac{p^{\mathrm{ga}}}{p^{\mathrm{c}}}\right)\right)\\
&+\mathrm{div}\left(\rho^{\mathrm{ga}}\frac{\boldsymbol{k}k^{\mathrm{rg}}}{\mu^{\mathrm{g}}}\left[-\mathrm{grad}(p^{\mathrm{g}})+\rho^{\mathrm{g}}\boldsymbol{g}\right]\right)=0
\end{aligned}\tag{3}$$

where p^{ga} is pressure of dry air. ρ^{ga} is the density of the dry air. μ^g is viscosity of gas phase; $\boldsymbol{D}$ is the effective diffusivity tensor expressed as follows:

$$D=n(1-S_{\mathrm{w}})\tau D_0\left(\frac{T}{T_0}\right)^{1.8}\frac{p_0}{p^{\mathrm{g}}}\tag{4}$$

where τ is tortuosity of the porous media. D_0 is diffusion coefficient of the vapor at the reference temperature T_0=273.15K and pressure p_0=101325Pa, D_0=2.58×10^{-5} m^2/s.

The density of the vapor can be presented using an empirical function (Rutqvist et al. 2001):

$$\rho^{\mathrm{gw}}=10^{-3}\mathrm{e}^{19.891-4975/T}\mathrm{e}^{-p^{\mathrm{c}}M_{\mathrm{w}}/(\rho^{\mathrm{w}}RT)}\tag{5}$$

The partial pressure of vapor, p^{gw} could be obtained according to Dalton's law:

$$p^{\mathrm{gw}}=\rho^{\mathrm{gw}}RT/M_{\mathrm{w}}\tag{6}$$

Then, the relationship between the matric suction and saturation of water is described using the van Genuchten model (van Genuchten 1980):

$$p^{\mathrm{c}}=p_0(S_{\mathrm{e}}^{\,m/(1-m)}-1)^{1/m}\tag{7}$$

$$S_{\mathrm{e}}=\frac{S_{\mathrm{w}}-S_{\mathrm{wr}}}{1-S_{\mathrm{wr}}-S_{\mathrm{gr}}}\tag{8}$$

where p^0 is gas entry pressure; S_e is effective saturation, and S_{wr} and S_{gr} are residual saturation for water and gas, respectively; m is a fitting parameter for van Genuchten model.

The relative permeabilities for water and gas phases are expressed as:

$$k^{\mathrm{rw}}=S_{\mathrm{e}}^{\,1/2}\left[1-\left(1-S_{\mathrm{e}}^{\,m/(m-1)}\right)^{(m-1)/m}\right]^2\tag{9}$$

$$k^{\mathrm{rg}}=(1-S_{\mathrm{e}})^{1/2}(1-S_{\mathrm{e}}^{\,m/(m-1)})^{2(1-1/m)}\tag{10}$$

Finally, the energy balance equation of the unsaturated medium is (Kolditz et al. 2012) written as:

$$\begin{aligned}
&C^{\mathrm{w}}\rho^{\mathrm{w}}\frac{\boldsymbol{k}k^{\mathrm{rw}}}{\mu^{\mathrm{w}}}[-\mathrm{grad}(p^{\mathrm{g}})+\mathrm{grad}(p^{\mathrm{c}})+\rho^{\mathrm{w}}\boldsymbol{g}]\mathrm{grad}(T)\\
&+C^{\mathrm{g}}\rho^{\mathrm{g}}\frac{\boldsymbol{k}k^{\mathrm{rg}}}{\mu^{\mathrm{g}}}[-\mathrm{grad}(p^{\mathrm{g}})+\rho^{\mathrm{g}}\boldsymbol{g}]\mathrm{grad}(T)\\
&+C\rho\frac{\partial T}{\partial t}-\mathrm{div}(\boldsymbol{\lambda}\mathrm{grad}(T))=q_{\mathrm{th}},
\end{aligned}\tag{11}$$

where $C\rho$ is heat capacity of the porous medium, $C\rho=nS_{\mathrm{w}}C^{\mathrm{w}}\rho^{\mathrm{w}}+n(1-S_{\mathrm{w}})C^{\mathrm{g}}\rho^{\mathrm{g}}+(1-n)C^{\mathrm{s}}\rho^{\mathrm{s}}$, in which C^w, C^g and C^s are specific heat capacities of water, gas, and solid, respectively; λ is heat conductivity of the porous medium, $\lambda=nS_{\mathrm{w}}\lambda^{\mathrm{w}}+n(1-S_{\mathrm{w}})\lambda^{\mathrm{g}}+(1-n)\lambda^{\mathrm{s}}$, in which λ^w, λ^g and λ^s are heat conductivities of water, gas, and solid, respectively.

3.2 *Numerical model and analysis conditions*

A one-dimensional thermo-hydraulic coupled numerical model was established using OpenGeoSys to investigate the thermally induced moisture movement in the loess layer. The geometric model was 0.9 m in height and 0.1 m in length, and the mesh size was 0.01 m×0.01 m. The initial matric suction of the model was 150 kPa. The initial gas pressure was set to be the atmospheric pressure of 101325 Pa. A constant temperature of 20℃ was employed to the top boundary, and several different temperatures were applied to the bottom boundary, namely 20, 40 and 60℃. Due to the capillary break at the interface of loess and gravel, the loess layer could store more water and percolation will occur when the bottom of the loess approximately reaches saturated, and thus the bottom boundary was assumed to be impervious for both water and gas phases. The top boundary was pervious for the gas phases. Particularly, a specific evaporation boundary was applied to the top boundary. The rate of evaporation can be calculated as reference to Song et al (2014) (see Eq. (12)). The simulation duration for all analysis conditions were 1 year, i.e., 365 days.

$$E_{\mathrm{a}}=(a+b\cdot n_{\mathrm{wind}})(1-H_{\mathrm{r}})\frac{H_{\mathrm{s}}-H_{\mathrm{r}}}{1-H_{\mathrm{r}}}\tag{12}$$

where E_a is evaporation rate; H_s is relative humidity of the surface soil; H_r is relative humidity of the air, which was taken as 0.1 in this study; n_{wind} is the wind speed, which was neglected in this study; a and b are empirical parameters of the empirical function. a was taken as 0.02 and b was considered as 0 as reference to Liu et al (2016).

On the other hand, to simulate the influence of vapor condensation on increasing the water storage in the cover, a water flux boundary was applied to the bottom of the model. According to the results from Eklund et al (1998), the LFG emission rate ranged from 0-70g/m^2/hr. Based on the results shown in Fig. 3, the water flux caused by the vapor condensation

could be obtained via multiplying the difference of the vapor content of the LFG between the bottom and surface of the cover by the LFG emission rate. The results of calculated water flux are shown in Table 1. The other initial and boundary conditions as well as the simulation duration were the same with the models previously mentioned.

Table 1 Parameters for the boundary conditions

Top temperature (℃)	Bottom temperature (℃)	Bottom water flux (10^{-10} m/s)
20	20	0-0.31
	40	0-2.78
	60	0-9.26

4 SOIL PROPERTIES

The properties of the material in this numerical model were the same with the compacted loess used in cover with a dry density of 1.45 g/cm^3. The soil water characteristics curve of the loess was measured using a 15-bar pressure plate extractor and best fitted using van Genuchten equation as shown in Fig. 4. The saturated hydraulic conductivity of the compacted loess was 2×10^{-7} m/s which was obtained using the falling-head method in the laboratory. The hydraulic conductivity curve was predicted based on the van Genuchten-Mualem model as shown in Fig. 5. It should be noted that the hysteresis was neglected in this paper. Other necessary parameters of material for the numerical modelling are listed in Table 2.

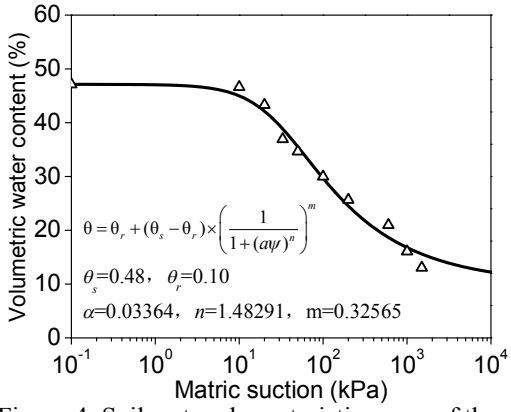

Figure 4. Soil water characteristic curve of the material

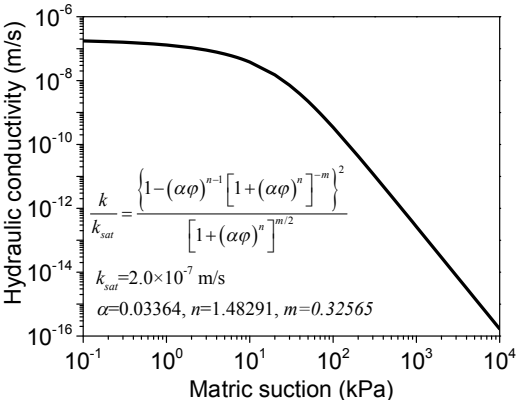

Figure 5. Hydraulic conductivity curve of the material

Table 2. Summary of material parameters for numerical modelling

Parameter	Value
Porosity, n	0.466
Parameter of van Genuchten model, p_0 (Pa)	31400
Heat conductivity of soil, λ^s (W/(m·K))	0.26
Heat conductivity of water, λ^w (W/(m·K))	0.6
Heat conductivity of gas, λ^g (W/(m·K))	0.026
Specific heat capacity of soil, C^s (J/(kg·K))	1600
Specific heat capacity of water, C^w (J/(kg·K))	4200
Specific heat capacity of gas, C^g (J/(kg·K))	1010

5 RESULTS

5.1 *Thermally induced moisture movement in the cover*

Figure 6 shows the distribution of the saturation of the cover at varying times. The temperature at the bottom and top were 60 and 20℃, respectively. It can be seen that the moisture in the cover transferred from the high-temperature zone to the low-temperature zone under thermal gradient. The water content decreased in the lower part of the cover and increased in the upper part, leading to the redistribution of water. On the 100th day after the simulation began, the saturation at the bottom of the cover decreased by 0.23, and the saturation at height between 0.3-0.6m increased by 0-0.02 compared with initial values. Due to the evaporation at the top boundary, the saturation at the height between 0.6-0.9m gradually decreased with the increasing time. Eventually, the saturation at height between 0.3-0.6m decreased less than its initial value on the 365th day attributed to the evaporation.

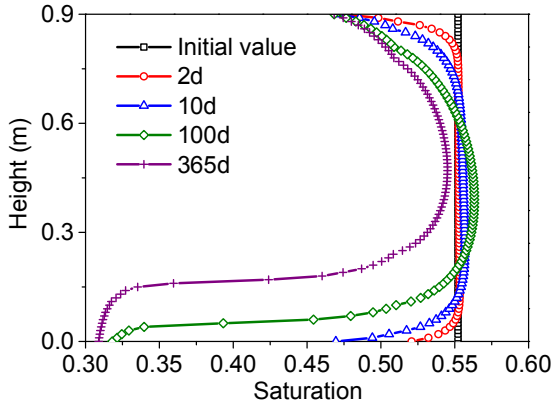

Figure 6. Saturation distribution of the cover at varying times

The properties of the thermally induced moisture movement in the cover could also be revealed by the development of the gas pressure distribution. It can be found from Fig. 7 that the gas pressure at any height was greater than the initial pressure during the whole simulation, which indicated the vaporization occurred caused by thermal gradient. As a whole, the gas pressure gradually decreased from the bottom to the surface of the cover, indicating that more vaporization happened in the zone with higher temperature

and vapor transferred from the higher temperature zone to the lower temperature zone. As the increase of the time, the gas pressure at the bottom of the cover gradually decreased and the saturation tended to reach a steady value, which indicated the rate of vaporization decreased.

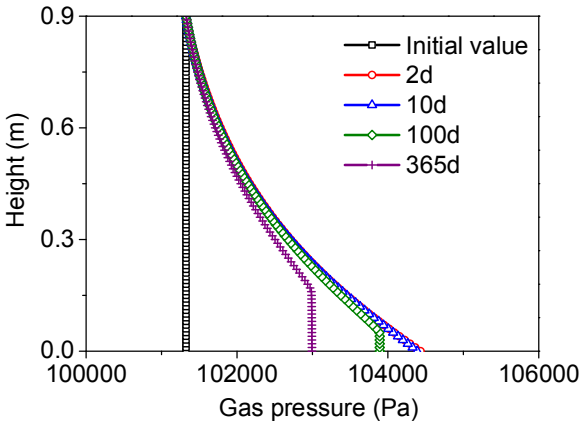

Figure 7. Gas pressure distribution of the cover at varying times

5.2 *Influence of varying thermal gradients on water storage in the cover*

Figure 8 shows the saturation distribution of the cover subjected to varying thermal gradients on the 365th day after the simulation began. For the case that the bottom temperature of the cover equaled 60℃, the saturation at the bottom of the cover decreased from 0.55 to 0.31, and the saturation at height between 0.3-0.9m increased by 0-0.03 compared with no thermal gradient (20-20℃). For the case with bottom temperature of 40℃, the saturation at the bottom of the cover decreased from 0.55 to 0.42, and no increase of the saturation appeared at height between 0.3-0.9m. This demonstrated that larger thermal gradient caused more moisture movement in the cover. The development of the available water storages in the cover under varying thermal gradient is presented in Fig. 9 (the method to calculate the available water storage could be found in Zhan et al (2016)). It can be seen that the increase of thermal gradient leaded to the decrease of available water storage in the whole cover (0-0.9m). Compared with the case under no thermal gradient, the water storage for the cover with the bottom temperature of 60℃ decreased by 15.7 mm on 365th day after the simulation began, amounting to 19% of the total available water storage. In addition, as previously mentioned, more moisture movement occurred due to the increasing thermal gradient, which will lead to more condensation at the upper part of the cover. Consequently, the available water storage in the cover at height between 0.3-0.9m for the case under maximum thermal gradient (60-20℃) was significantly larger than other cases during the whole simulation. However, larger water storage in the upper part of the cover caused larger evaporation, and so the water storage in the whole cover (0-0.9m) was the least for the case under maximum thermal gradient.

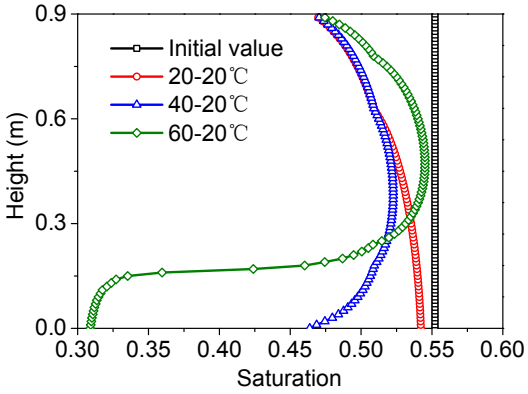

Figure 8. Saturation distribution of the cover subjected to varying thermal gradients (365d)

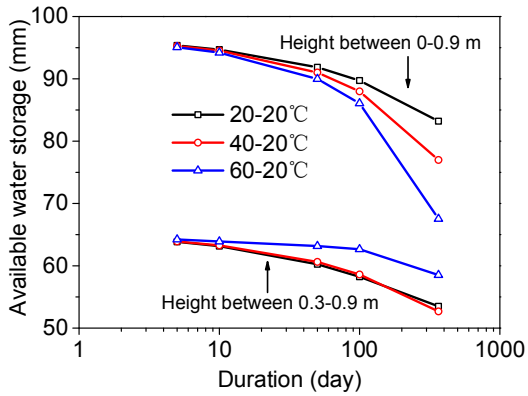

Figure 9. Development of the available water storages in the cover subjected to varying thermal gradients

5.3 *Influence of vapor content of the LFG on water storage in the cover*

Figure 10 shows the comparison of the saturation distribution between the case with and without considering vapor content of the LFG (on the 365th day, the bottom temperature was 40℃). It can be found from Fig. 10 that the water content of the cover increased after considering the vapor of the LFG. The increase of the water content caused by the vapor decreased from the bottom to the surface of the cover. The available water storages in the cover on the 365th day subjected to varying vapor contents under different thermal gradients are shown in Fig. 11. The varying vapor contents included $0q_{max}$, $0.1q_{max}$, $0.5q_{max}$ and $1q_{max}$ under corresponding thermal gradient, where q_{max} is the maximum water flux as shown in Table 1. The vapor content (water flux) was normalized by the maximum water flux as shown in Fig. 11. It can be seen that the water storage in the cover increased with the increase of the normalized water flux for a given thermal gradient. Furthermore, the larger thermal gradient, the larger increase rate of the water storage with the increase of the normalized water flux, which was attributed to the larger vapor content of the LFG caused by higher temperature. For the case of the cover with no thermal gradient, the maximum increase of the available water storage for a whole year was 1.1 mm. While, for the case

with the bottom temperature of 60℃, the maximum increase of the available water storage for a whole year was 30 mm.

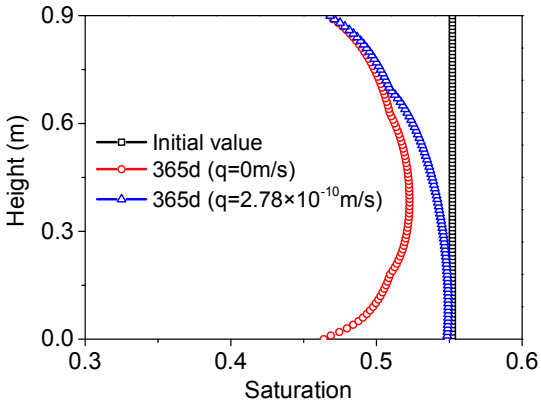

Figure 10. Saturation distribution of the cover (365d, 40-20℃)

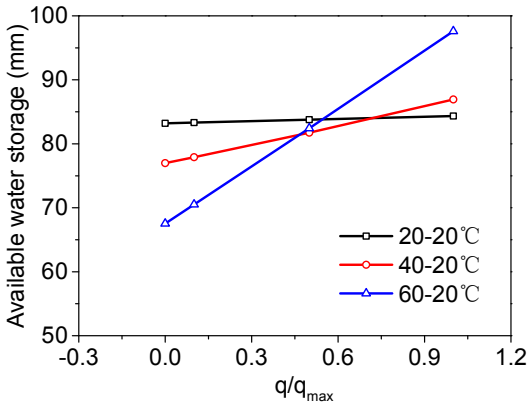

Figure 11. Available water storages in the cover subjected to varying vapor contents (365d)

6 CONCLUSIONS

In this study, the temperature and relative humidity of the LFG at the bottom and surface of the loess-gravel cover were measured. Based on the field measurements, the numerical simulations were carried out to investigate the influence of the thermal gradient and vapor content of the LFG on water storage in the cover. The following conclusions can be drawn:

1) Moisture transferred from the higher-temperature zone to the lower-temperature zone by means of vaporization and condensation due to thermal gradient, leading to the redistribution of water. Larger thermal gradient caused more moisture movement in the cover. The increase of the water storage in the upper part of the cover can accelerate the evaporation at the cover surface, which could in turn decrease the water storage in the whole cover. The maximum decrease of the available water storage caused by thermal gradient for a whole year was 16 mm.
2) The water content of the cover increased after considering the vapor in the LFG. The increase of the water content caused by the vapor decreased from the bottom to the surface of the cover. The larger thermal gradient, the larger increase rate of the water storage with the increase of the normalized water flux. The maximum increase of the available water storage caused by the vapor content of LFG for a whole year was 30 mm.

7 ACKNOWLEDGEMENTS

The authors acknowledge financial support from the National Science Fund for Distinguished Young Scholars (No. 51625805).

8 REFERENCES

Brachman, R.W.I., Rentz, A., Rowe, R.K., & Take, W.A. 2014. Classification and quantification of downslope erosion from a geosynthetic clay liner (GCL) when covered only by a black geomembrane. *Canadian Geotechnical Journal*, 52(4): 395-412.

Dach, J. & Jager, J. 1995. Prediction of gas and temperature with the disposal of pretreated residential waste. *Proceedings of 5th International Waste Management and Landfill Symposium, CISA, Italy*, I: 665-677.

Eklund, B., Anderson, E.P., Walker, B.L. & Burrows, D.B. 1998. Characterization of landfill gas composition at the fresh kills municipal solid-waste landfill. *Environmental Science & Technology* 32(15): 2233-2237.

Kolditz, O., Görke, U., Shao, H.B. et al. 2012. Thermo-Hydro-Mechanical-Chemical Processes in Porous Media. *Springer, Berlin Heidelberg, Germany*, p.89.

Li, Q., Yao, Y. P., & Han, L. M et al. 2014. Pot-cover effect of soil. *Industrial Construction* 44(2): 69-71. (in Chinese)

Liu, X.C., Xu, W.J., Zhan, L.T. & Chen, Y.M. 2016. Laboratory and numerical study on an enhanced evaporation process in a loess soil column subjected to heating. *Journal of Zhejiang University-SCIENCE A* 17(7): 553-564.

Mbonimpa, M., Aubertin, M., Aachib, M. & Bussière, B. 2003. Diffusion and consumption of oxygen in unsaturated cover materials. *Canadian Geotechnical Journal* 40(5): 916-932.

Rutqvist, J., Börgesson, L., Chijimatsu, M. et al. 2001. Thermohydromechanics of partially saturated geological media: governing equations and formulation of four finite element models. *International Journal of Rock Mechanics and Mining Sciences* 38(1): 105-127.

Sanavia, L., Pesavento, F. & Schrefler, B.A. 2005. Finite element analysis of non-isothermal multiphase geomaterials with application to strain localization simulation. *Computational Mechanics* 37(4): 331-348.

Song, W.K. 2014. Experimental investigation of water evaporation from sand and clay using an environmental chamber. *PhD Thesis, Université Paris-Est, Paris, France*.

Spokas, K. A. & Bogner, J. E. 2011. Limits and dynamics of methane oxidation in landfill cover soils. *Waste Management* 31(5): 823-832.

van Genuchten, M.T. 1980. A closed-form equation for predict-ing the hydraulic conductivity of unsaturated soils. *Soil Science Society of America Journal* 44(5): 892-898.

Zhan, T.L.T., Li, G., Jiao, W., Wu, T., Lan, J. & Chen, Y.M. 2016. Field measurements of water storage capacity in a loess/gravel capillary barrier cover using rainfall simulation tests. *Canadian Geotechnical Journal,* https://doi.org/10.1139/cgj-2016-0298